

Long-range transport of 2D excitons in dynamic acoustic lattice

Ruoming Peng¹, Adina Ripin², Yusen Ye³, Jiayi Zhu², Changming Wu¹, Seokhyeong Lee¹, Huan Li^{1,*}, Takashi Taniguchi⁴, Kenji Watanabe⁴, Ting Cao³, Xiaodong Xu^{2,3}, Mo Li^{1,2,†}

¹*Department of Electrical and Computer Engineering, University of Washington, Seattle, WA 98195, USA*

²*Department of Physics, University of Washington, Seattle, WA 98195, USA*

³*Department of Material Science and Engineering, University of Washington, Seattle, WA 98195, USA*

⁴*Research Center for Functional Materials, National Institute for Materials Science, Tsukuba, Japan*

ABSTRACT:

Excitons are elementary optical excitation in semiconductors. The ability to manipulate and transport these quasiparticles would enable excitonic circuits and devices for quantum photonic technologies. Recently, interlayer excitons in 2D semiconductors have emerged as a promising candidate for engineering excitonic devices due to long lifetime, large exciton binding energy, and gate tunability. However, the charge-neutral nature of the excitons leads to a weak response to the in-plane electric field and thus inhibits transport beyond the diffusion length. Here, we demonstrate the directional transport of interlayer excitons in bilayer WSe₂ driven by the dynamic potential lattice induced by surface acoustic waves (SAW). We show that at 100 K, the SAW-driven excitonic transport is activated above a threshold acoustic power and reaches a distance at least ten times longer than the diffusion length, only limited by the device size. Temperature-dependent measurement reveals the transition from the diffusion-limited regime at low temperature to an acoustic field-driven regime at elevated temperature. Our work shows that acoustic waves are an effective, contact-free means to control exciton dynamics and transport, promising for realizing 2D materials-based excitonic devices such as exciton transistors, switches, and transducers.

* Present Address: Zhejiang University, China

† Email: moli96@uw.edu

Excitons in semiconductor systems can be optically excited and read out, thereby encoding and storing optical signals into the excitons' spin, valley, and orbital degrees of freedom¹⁻⁴. In analogous to electronic circuits, circuits with excitons as the active information carriers have been envisioned, which transport and manipulate excitonic states with applied electrical and magnetic fields^{5,6}. Transducing between photons and solid-state media, such excitonic circuits can directly process optical signals and regenerate light without additional optical-electrical conversions so that they can be very efficient⁶. However, unlike electrons or holes, charge-neutral excitons experience no net force under uniform electric fields. They can also be dissociated by a moderately strong in-plane electric field if the binding energy is small^{7,8}. Therefore, diffusion is one of the main mechanisms for exciton motion⁹⁻¹³. For example, in GaAs quantum well systems, the high mobility of exciton has enabled 10s of microns diffusion length at low temperature¹⁴⁻¹⁷. To actively transport excitons with controlled directionality, surface acoustic waves (SAW) have also been employed as an effective means to transport excitons in GaAs quantum well systems¹⁴⁻¹⁸. Over 100s of microns transport distance is achieved at a temperature below $< 4\text{K}$ ^{15,16}. However, the low exciton binding energy in GaAs prohibits higher temperature operation is not possible¹⁹.

In contrast, excitons in 2D transition metal dichalcogenides (TMDCs) (e.g., MoS₂, MoSe₂, WS₂, WSe₂) have binding energy approaching a fraction of an electron volt^{3,4} and strong resonances even at room temperature²⁰⁻²³, making them promising for a plethora of optoelectronic and quantum applications²⁴⁻²⁸. Particularly, for realizing exciton circuits, the indirect excitons (IXs) in bilayers and heterobilayers of TMDCs have additional desirable properties^{27,29-32}. Because these IXs consist of electrons and holes separated in different layers and valleys, their population lifetimes at low temperature are up to 100s of nanoseconds⁴, facilitating long-range transport before exciton relaxation. Importantly, IXs have a permanent perpendicular dipole moment so that their energy can be tuned with an out-of-plane electric field^{33,34}, and they can be driven by a lateral electric-field gradient³⁵. Indeed, a prototypical TMDC excitonic transistor has been demonstrated based on the IX diffusion in MoSe₂/WSe₂ heterobilayers³⁵⁻³⁷. The application of an out-of-plane static electric field creates an energy barrier or a trap for IX. Thus, switching on and off the electric field can suppress or enable exciton diffusion³⁷. However, due to limited exciton mobility³⁸, both diffusive and repulsive transports of IXs can only achieve a transport distance of a few μm with milliwatts of pump power at a low temperature³⁹. More importantly, such transport based on free

or repulsive diffusion is non-directional, thus challenging to realize sophisticated excitonic circuits, which entail transport of excitons in a controlled direction over a long distance.

Here, we demonstrate the long-range and directional transport of IXs in a bilayer WSe₂ using SAW at temperatures up to RT. The IXs in a bilayer WSe₂ are momentum indirect with a long lifetime of up to 10 ns at 10 K and \sim 1 ns even at RT^{29,37}. It was reported recently that the exciton energy of IXs in bilayer WSe₂ could be modulated by an out-of-plane static field²⁹. Consider a bilayer WSe₂ placed directly on a piezoelectric substrate (Fig. 1a). SAW is excited and propagates through the area where a bilayer WSe₂ is transferred to. On a piezoelectric substrate such as LiNbO₃, the propagating SAW will generate a near-field piezoelectric field with a large out-of-plane field (E_z) amplitude on the order of 10^7 V/m at 1 mW/ μ m of acoustic power. As such, the E_z component will periodically modulate the IX energy in space and time, creating a dynamic lattice of trapping potential for the IXs in the extrema of E_z . As the SAW propagates, the IXs will drift along the gradient of E_z and thus be carried by the SAW—like surfing on a wave—to travel a long distance before they recombine (Fig. 1b). With a SAW velocity of $>3\times10^3$ m/s and an exciton population lifetime >10 ns, the IXs can travel >30 μ m, an order of magnitude longer than the distance diffusion can reach.

Fig. 1b depicts the scenario when a bilayer WSe₂ is under both optical pumping and SAW modulation. Since the bilayer WSe₂ is inversion symmetric, there are two energy degenerate IXs with dipole moment p pointing along the $+z$ and $-z$ directions, respectively. For simplicity, hereon, we use $+z$ IX to explain the transport process. The electric field $E(r, t)$ induced by the SAW modulates the IX energy by $\Delta E = -p \cdot E$ and thus creates a dynamic potential well moving at the acoustic velocity. At low temperatures, the optically excited IXs will quickly relax to the energy minimum created by the SAW in real space and travel with the propagating SAW. Fig. 1c shows the optical image of our device. We designed a focusing IDT structure that focuses the acoustic wave into the WSe₂ region to concentrate the acoustic power density and enhance the piezoelectric field E . The IDT excites a strong SAW mode at 1.237 GHz with an acoustic wavelength of 2.832 μ m, assuming an acoustic velocity of 3.5×10^3 m/s for the z-propagating Rayleigh mode in a y-cut LiNbO₃ (see S.I). Fig. 1d shows the simulated electric field profile of the focused acoustic wave, which at the focal point has a waist of \sim 3.0 μ m. To reduce the inhomogeneous broadening and exciton trapping from spatial variation of surface potential, we encapsulated the bilayer WSe₂ with

~10 nm hexagonal boron nitride (h-BN) flakes using the standard pick-up method and transferred onto the LiNbO_3 substrate with pre-patterned IDTs⁴⁰. A thin layer of indium-tin-oxide (ITO) was deposited on the heterostructure region as a top transparent electrode. This top electrode plays an important role by efficiently suppressing the in-plane field component (E_x), which may cause exciton dissociation^{17,41} while maintaining a relatively strong out-of-plane component of the piezoelectric field E_z . The finite-element method (FEM) simulation (Fig. 1e, f) shows that the ITO layer suppresses E_x by about two orders of magnitude.

We first demonstrate efficient SAW-driven transport of IXs by performing spatially resolved photoluminescence (PL) measurement. Without SAW and at a low pump power, the diffusive IX flux density can be described by the diffusion equation: $j = -D\nabla N$, where D is the temperature-dependent diffusion coefficient and N is the exciton density (inset, Fig. 1a). Due to the low D in TMDC, the IX diffusion is relatively weak. In comparison, when SAW is turned on, the IX dynamics is strongly modulated by the piezoelectric field and drift along the SAW propagation direction (inset, Fig. 2b). As the velocity of the SAW (~3000 m/s) is much smaller than the thermal velocity of excitons ($10^4 - 10^5$ m/s in our experimental condition, see SI), the IXs can be treated as an exciton gas in quasi-equilibrium. With sufficiently high SAW amplitude, the IX gas will be trapped in the energy minimum of SAW and drift with the center-of-mass velocity identical to the SAW velocity.

Figures 2a and b compare the PL images measured at 100 K with SAW off and on, respectively. The IXs were excited with a He-Ne laser at 633 nm, having a power of $P_p=20 \mu\text{W}$, and focused to a diffraction-limited spot size of 1 μm near the edge of the WSe_2 flake close to the IDT. Without SAW (Fig. 2a), the IXs diffuse by only 1-2 microns, consistent with previous measurement results. When SAW is turned on with power $P_s=6 \text{ mW}$, as shown in Fig. 2b, we observe strong exciton emission at two spots on the far edge of the WSe_2 flake, along the SAW propagation direction and ~20 μm away from the pump spot. The two separate emission spots are at the corners (one convex and one concave) of the flake edge and are related to the SAW wavefront at the flake boundary (Fig. 1d). The IXs are transported at the acoustic velocity of $3.5 \times 10^3 \text{ m/s}$ so the traveling time is less than 6 ns, shorter than the lifetime²⁹. The results reveal SAW-driven transport of IXs over a device size limited distance, setting a lower bound of the propagation length to ~20 μm .

To confirm the transport is indeed from IXs, we performed spatially and energy resolved measurements. We aligned the slit of the spectrometer with the SAW propagation direction (y-axis) and acquired spectral PL images with SAW off and on (Figs. 2c and d). The emission of the transported IXs is predominantly at the energy around 1.56 eV, which agrees with the IX energy of bilayer WSe₂^{29,42,43}. The result is consistent with our expectation that only IXs with perpendicular dipole moment are efficiently transported by SAW. At the pump spot (Fig. 2e), the IX emission slightly decreases when SAW is turned on, presumably due to the removal of IXs by the SAW. In contrast, at the far edge of the flake (Fig. 2f), the application of SAW increased the emission intensity by more than 20-fold. We can confidently rule out the contribution of free carriers to the observed non-local excitonic emission. To dissociate IXs to free carriers, an in-plane field of more than 5×10^6 V/m is needed⁴⁴, much higher than the E_x of the piezoelectric field induced by the SAW (Fig. 1f). In Figs. 2b and d, there is also an appreciable emission increase in the area between the pump spot and the flake edge when SAW is on. The emission is attributed to transported IXs rather than dissociated free carriers. If there are also free electrons and holes transporting along the SAW direction, they will not recombine because electrons and holes are trapped at different acoustic field extrema.

We next characterize the IX transport at different SAW powers P_s . We find that the transported excitons grow monotonically with the SAW power, but the trend is highly nonlinear with an activation behavior. For $P_s < 3.0$ mW, the IX transport is negligible, and the IX emission is localized near the laser excitation spot (Fig. 3a). When P_s goes above 3.0 mW and increases to 4.5 mW, two bright emission spots at the flake edge appear, suggesting efficient activation of the transport process (Fig. 3b). When further increasing P_s to 6 mW, the exciton transport becomes so efficient that the emission intensity at the flake edge is already comparable to that at the pump spot (Fig. 3c). Fig. 3d plots the integrated emission intensity at the flake edge, which is proportional to the transported exciton density n_T , as a function of P_s . The experimental result agrees with our theoretical model of SAW activated transport in which the transported exciton density n_T is proportional to $e^{\sqrt{P_s/P_t}}$ at a given temperature (see SI). Fitting the result at 100 K gives a relatively small $P_t \sim 0.1$ mW, beyond which the excitons can respond to the piezoelectric field induced by the SAW. Similar exponential behavior and power law has also been observed in coupled GaAs quantum wells¹⁴, where exciton transport is impeded by disorder and defect-induced potential

variation at the low SAW power limit. In TMDC such as bilayer WSe₂, intrinsic defect density can be $>7.0 \times 10^{10} \text{ cm}^{-2}$, along with the potential variation induced by local strain caused by the transfer process⁴⁰. For efficient IX transport to happen, the SAW modulation of IX energy ΔE needs to overcome the potential variation by the local defects and strain (see SI), and the efficiency of exciton transport is sensitive to the material quality and the fabrication process.

The activation behavior motivates us to further measured SAW-driven IX transport at different temperatures. Fig. 4 shows the spectral PL mapping at temperatures from 6 K to 200 K with pump power $P_p=20 \mu\text{W}$ and SAW power $P_s = 6 \text{ mW}$. Rich features have been obtained, showing dominant roles of exciton localization, SAW-driven transport, recombination and phonon scattering at different temperature ranges. Note that measurement in each temperature is normalized to its respective maxima for clarity. At 6 K and with SAW off, the emission spectrum shows a series of sharp resonances (Fig. 4a) attributed to defect emission and phonon-assisted recombination of the IXs. When SAW is on, the sharp resonances disappear, and the emission intensity decreases significantly (Fig. 4b and SI). Meanwhile, IX transport at this low temperature is very weak. The suppression of IX emission can be explained by the effect that the SAW reduces the coupling between excitons and recombination centers such as defects. When the temperature increases to 30 K, the sharp exciton resonances disappear even without SAW (Fig. 4c). At this elevated temperature range, the excitons are thermalized into exciton gas, leading to weaker couplings with the local defects. As a result, the SAW-driven transport starts to make the PL at the flake's edge observable (Fig. 4d). When the temperature reaches 100 K, the IX emission becomes more than two times brighter at the pump spot (Fig. 4e) because indirect IX recombination becomes more efficient when the thermal phonon density is high. The SAW-driven transport is also the most prominent at this temperature (Fig. 4f) because of the negligible role of disorder and surface potential variation compared to the SAW modulation and the relatively long exciton population lifetime, which allows for the transport of IX to the edge without significant decay. At 200 K (above the Debye temperature), the bilayer WSe₂ develops sizable acoustic and optical phonon populations. As a result, IX emission has a broad spectrum and high intensity without SAW (Fig. 4g). However, the IX transport is impeded due to strong exciton-phonon scattering and decreased exciton population lifetime (Fig. 4h). Overall, our systematic measurements have revealed three regimes of IX behaviors and the transition between them. At the lowest temperatures,

the IXs are highly localized and transported is diffusion-limited. At intermediate temperatures, the IXs are bright with phonon-assisted recombination. At the same time, they still have a long lifetime, allowing for efficient SAW-driven transport over a long distance. At further elevated temperatures, strong phonon scattering decreases exciton mobility and lifetime, impeding efficient exciton transport. Nevertheless, thanks to the strong SAW modulation, even at room temperature, we still observe a SAW-driven transport distance of $\sim 2.0 \mu\text{m}$ (see SI).

In conclusion, we have demonstrated that SAW is an efficient, contact-free approach to transport IXs in bilayer WSe₂ over a distance far beyond the diffusion length. The SAW-driven transport happens when the SAW modulation of IX energy can overcome the local potential variation and defect traps in the bilayer WSe₂ device. Since the transport distance depends on the exciton lifetime of the optically active material and the acoustic velocity of the substrate, using TMDCs with longer lifetimes and piezoelectric substrate with higher acoustic velocity can lead to a much longer transport distance. The contact-free transport driven by the acoustic wave that is launched remotely also preserves the high quality of the material system and prevents undesired spatial variations induced by local gates^{35–37,39}. Although the maximal transport distance is reached at the temperature of 100 K in the current device, we observe SAW transport even at room temperature. With improved material quality, especially pristine interfaces, the efficient room-temperature operation will be achievable. We note that SAW is a universal approach to control excitons, it can be applied to many other 2D material systems with different types of excitons, and both of its piezoelectric field and strain field can be utilized to manipulate and transport excitons. SAW can also be guided and circulated in phononic circuits and resonators^{45,46}, which will afford rich functionality and flexibility to manipulate and explore exciton physics.

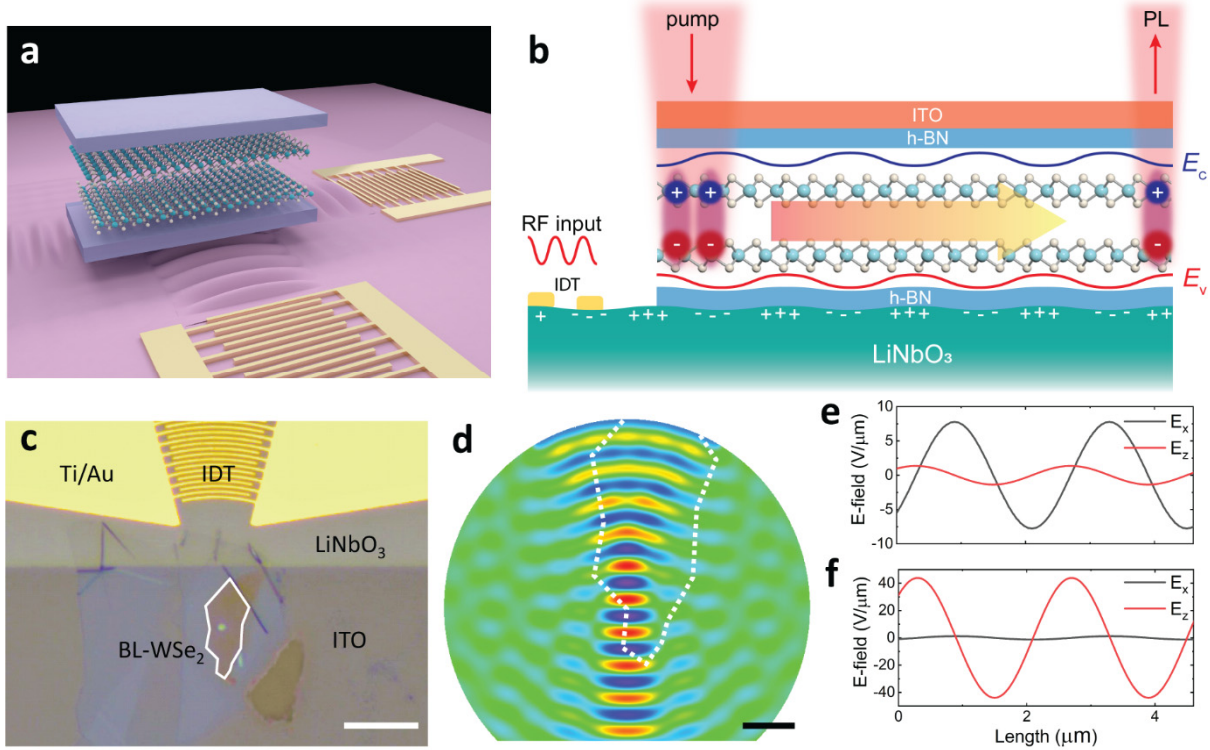


Fig.1 Integrating bilayer WSe₂ with SAW devices. **a.** Schematic illustration of the h-BN encapsulated bilayer WSe₂ stacked on a SAW device. The IDTs generate SAW to transport the excitons in the acoustic wave propagating directions. **b.** The propagating SAW periodically modulates the energy of the bound electrons and holes and transport excitons from the pump spot to the flake edge, where they recombine to generate photoluminescence. For simplicity, we only plot +z interlayer exciton in bilayer WSe₂. See supplementary materials for details. **c.** Optical microscope image of the device, with the white outline highlighting the bilayer WSe₂ region. Scale bar, 20 μ m. **d.** The piezoelectric field profile of the SAW generated by the focusing IDT. The acoustic focal point is in the bilayer WSe₂ region with a beam waist of 3 μ m. The dotted line outlines the WSe₂ flake. Scale bar, 5 μ m. **e-f,** The piezoelectric field distribution with (e) and without (f) the top ITO electrode. The field amplitude is calculated assuming an acoustic power density of 1mW/ μ m. The ITO electrode can efficiently suppress the in-plane component of the piezoelectric field, which causes undesirable exciton dissociation.

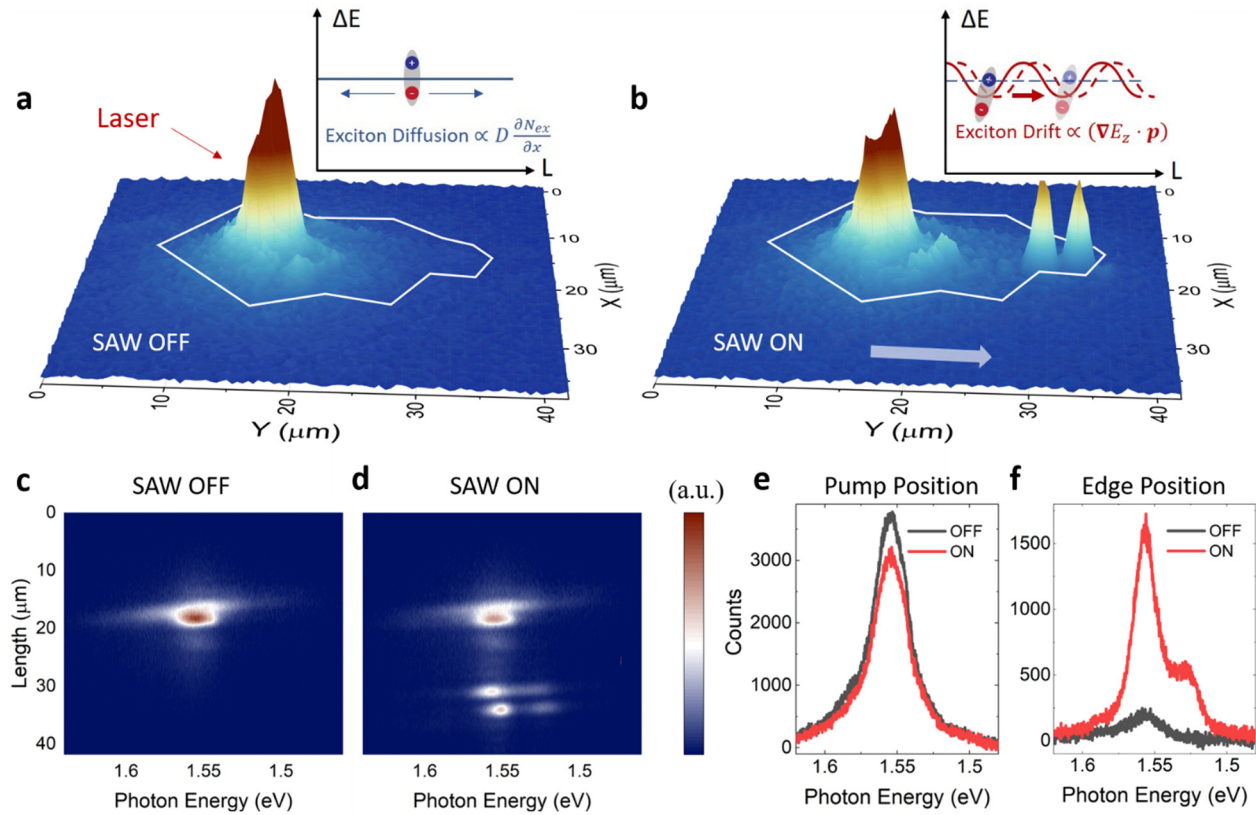


Fig 2. SAW-driven transport of IXs at 100 K. **a-b**, Real-space PL mapping (**a**), when SAW is off, and (**b**) when SAW is on with 6 mW power. Two bright emission spots appear at the edge of the flake and the focal point of the acoustic wave (see Fig. 1d) due to the SAW-driven transport of IXs. Insets: Illustration of free diffusion and SAW-driven drift of IXs. **c-d**, The spectral PL image at the same experimental conditions as **a-b**. The non-local exciton emission at the flake edge is clearly attributed to the IXs in WSe₂, which have an emission peak at 1.56 eV. **e**, The emission spectrum at the pump position slightly decreases when SAW is turned on. **f**, The emission spectrum at the flake edge position drastically increases when SAW is turned on.

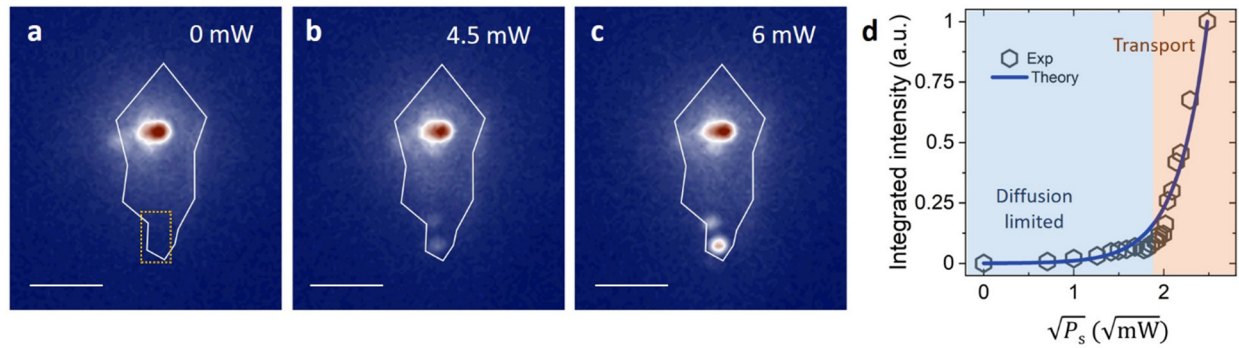


Fig 3. Acoustic power-dependent IX transport at 100 K. **a-c** PL images at different SAW power P_s of **(a)** 0 mW, **(b)** 4.5 mW, **(c)** 6 mW. The solid white line outlines the WSe₂ flake. The two bright emission spots at the edge of the WSe₂ flake highlight the SAW-driven transport of IXs. Scale bar, 10 μm . **d**, The integrated emission intensity at the flake edge (in the area indicated by the yellow dashed box in **a**) depending on the SAW power P_s . The experimental data is fitted with the theoretical model that the transport density exponentially depends on the square root of the acoustic power. With a low acoustic power, the exciton transport is diffusion limited (blue shaded). With a high SAW power, SAW-driven transport is activated (red shaded).

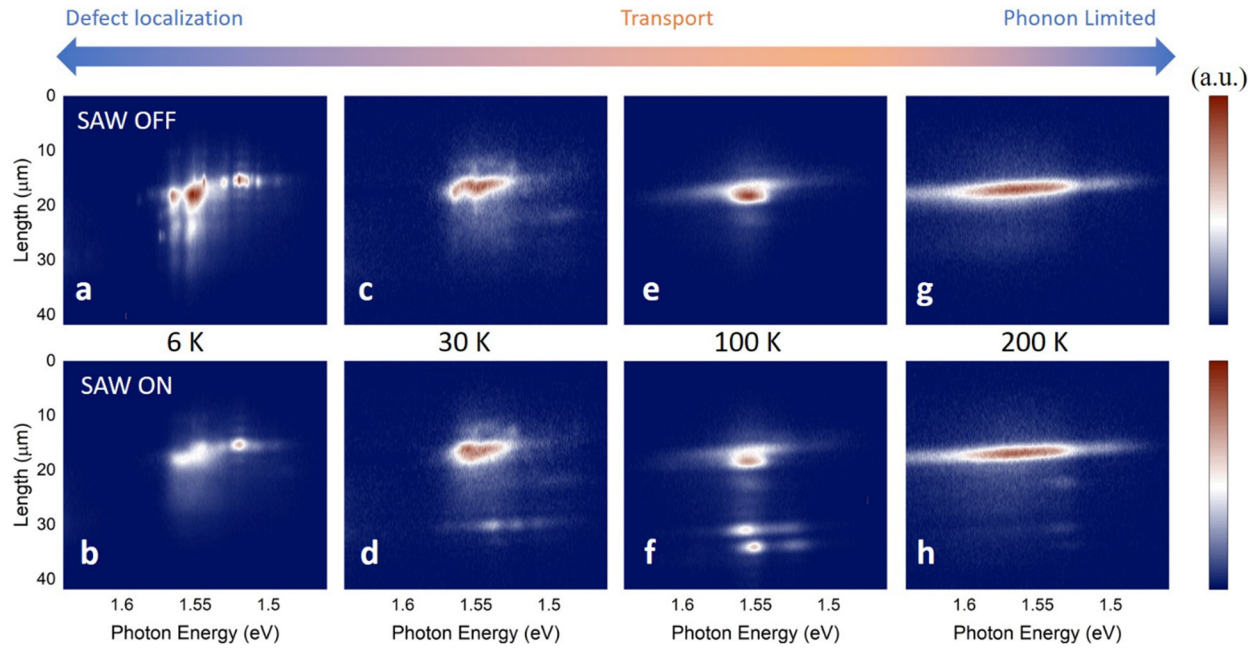


Fig 4. SAW-driven IX transport at varying temperatures. The spectral PL image of the exciton transport at 6-200 K with SAW off (a, c, e, g) and on (b, d, f, h). For clarity, the data measured at each temperature is normalized separately. **a, b,** At low temperature (6K), IXs show narrow peaks as they are highly localized to recombination centers such as defects or strongly couple to local vibrational modes. SAW can delocalize the IXs so to suppress emission. However, the transported IXs remain dark because the cold excitons cannot overcome potential variation. **c, d,** At elevated temperatures (30 K), the IXs are thermalized with broad emission. SAW transport turns up with visible emission at the flake edge. **e, f,** At 100 K, SAW transport of IXs is most prominent as IXs have a sufficiently long lifetime and can efficiently couple to SAW. **g, h,** At even higher temperature, SAW transport, although visible, is inefficient as exciton-phonon scattering dominates and the population lifetime of IXs is reduced.

Reference:

1. Miller, R. C., Kleinman, D. A., Tsang, W. T. & Gossard, A. C. Observation of the excited level of excitons in GaAs quantum wells. *Phys. Rev. B* **24**, 1134–1136 (1981).
2. Miller, R. C. & Kleinman, D. A. Excitons in GaAs quantum wells. *J. Lumin.* **30**, 520–540 (1985).
3. Schaibley, J. R. *et al.* Valleytronics in 2D materials. *Nat. Rev. Mater.* **1**, 16055 (2016).
4. Rivera, P. *et al.* Interlayer valley excitons in heterobilayers of transition metal dichalcogenides. *Nat. Nanotechnol.* **13**, 1004–1015 (2018).
5. Bar-Ad, S. & Bar-Joseph, I. Exciton spin dynamics in GaAs heterostructures. *Phys. Rev. Lett.* **68**, 349–352 (1992).
6. High, A. A., Novitskaya, E. E., Butov, L. V., Hanson, M. & Gossard, A. C. Control of exciton fluxes in an excitonic integrated circuit. *Science* **321**, 229–231 (2008).
7. Brum, J. A. & Bastard, G. Electric-field-induced dissociation of excitons in semiconductor quantum wells. *Phys. Rev. B* **31**, 3893–3898 (1985).
8. Massicotte, M. *et al.* Dissociation of two-dimensional excitons in monolayer WSe₂. *Nat. Commun.* **9**, 1633 (2018).
9. Hegarty, J., Goldner, L. & Sturge, M. D. Localized and delocalized two-dimensional excitons in GaAs-AlGaAs multiple-quantum-well structures. *Phys. Rev. B* **30**, 7346–7348 (1984).
10. Gärtner, A., Holleitner, A. W., Kotthaus, J. P. & Schuh, D. Drift mobility of long-living excitons in coupled GaAs quantum wells. *Appl. Phys. Lett.* **89**, 052108 (2006).
11. Cadiz, F. *et al.* Exciton diffusion in WSe₂ monolayers embedded in a van der Waals heterostructure. *Appl. Phys. Lett.* **112**, 152106 (2018).
12. Kulig, M. *et al.* Exciton Diffusion and Halo Effects in Monolayer Semiconductors. *Phys. Rev. Lett.* **120**, 207401 (2018).
13. Javey, A. *et al.* Neutral exciton diffusion in monolayer MoS₂. *ACS Nano* **14**, 13433–13440

(2020).

14. Rocke, C. *et al.* Acoustically driven storage of light in a quantum well. *Phys. Rev. Lett.* **78**, 4099–4102 (1997).
15. Rudolph, J., Hey, R. & Santos, P. V. Long-range exciton transport by dynamic strain fields in a GaAs quantum well. *Phys. Rev. Lett.* **99**, 047602 (2007).
16. Violante, A. *et al.* Dynamics of indirect exciton transport by moving acoustic fields. *New J. Phys.* **16**, 033035 (2014).
17. Delsing, P. *et al.* The 2019 surface acoustic waves roadmap. *Journal of Physics D: Applied Physics* **52**, 353001 (2019).
18. Cerdá-Méndez, E. A. *et al.* Polariton condensation in dynamic acoustic lattices. *Phys. Rev. Lett.* **105**, 116402 (2010).
19. Tarucha, S., Okamoto, H., Iwasa, Y. & Miura, N. Exciton binding energy in GaAs quantum wells deduced from magneto-optical absorption measurement. *Solid State Commun.* **52**, 815–819 (1984).
20. Withers, F. *et al.* WSe₂ Light-Emitting Tunneling Transistors with Enhanced Brightness at Room Temperature. *Nano Lett.* **15**, 8223–8228 (2015).
21. Zhu, B., Chen, X. & Cui, X. Exciton binding energy of monolayer WS₂. *Sci. Rep.* **5**, 9218 (2015).
22. Lundt, N. *et al.* Room-temperature Tamm-plasmon exciton-polaritons with a WSe₂ monolayer. *Nat. Commun.* **7**, 13328 (2016).
23. Liu, Y. *et al.* Room temperature nanocavity laser with interlayer excitons in 2D heterostructures. *Sci. Adv.* **5**, eaav4506 (2019).
24. Xia, F., Wang, H., Xiao, D., Dubey, M. & Ramasubramaniam, A. Two-dimensional material nanophotonics. *Nat. Photonics* **8**, 899–907 (2014).
25. Wu, S. *et al.* Monolayer semiconductor nanocavity lasers with ultralow thresholds. *Nature* **520**, 69–72 (2015).

26. Zhang, L., Gogna, R., Burg, W., Tutuc, E. & Deng, H. Photonic-crystal exciton-polaritons in monolayer semiconductors. *Nat. Commun.* **9**, 713 (2018).
27. Wang, Z. *et al.* Evidence of high-temperature exciton condensation in two-dimensional atomic double layers. *Nature* **574**, 76–80 (2019).
28. Zhang, L. *et al.* Van der Waals heterostructure polaritons with moiré-induced nonlinearity. *Nature* **591**, 61–65 (2021).
29. Wang, Z., Chiu, Y. H., Honz, K., Mak, K. F. & Shan, J. Electrical Tuning of Interlayer Exciton Gases in WSe₂ Bilayers. *Nano Lett.* **18**, 137–143 (2018).
30. Seyler, K. L. *et al.* Signatures of moiré-trapped valley excitons in MoSe₂/WSe₂ heterobilayers. *Nature* **567**, 66–70 (2019).
31. Jin, C. *et al.* Observation of moiré excitons in WSe₂/WS₂ heterostructure superlattices. *Nature* **567**, 76–80 (2019).
32. Tran, K. *et al.* Evidence for moiré excitons in van der Waals heterostructures. *Nature* **567**, 71–75 (2019).
33. Rivera, P. *et al.* Observation of long-lived interlayer excitons in monolayer MoSe 2-WSe 2 heterostructures. *Nat. Commun.* **6**, 6242 (2015).
34. Peimyoo, N. *et al.* Electrical tuning of optically active interlayer excitons in bilayer MoS₂. *Nat. Nanotechnol.* **4**–10 (2021).
35. Unuchek, D. *et al.* Room-temperature electrical control of exciton flux in a van der Waals heterostructure. *Nature* **560**, 340–344 (2018).
36. Unuchek, D. *et al.* Valley-polarized exciton currents in a van der Waals heterostructure. *Nat. Nanotechnol.* **14**, 1104–1109 (2019).
37. Liu, Y. *et al.* Electrically controllable router of interlayer excitons. *Sci. Adv.* **6**, eaba1830 (2020).
38. Radisavljevic, B., Radenovic, A., Brivio, J., Giacometti, V. & Kis, A. Single-layer MoS₂ transistors. *Nat. Nanotechnol.* **6**, 147–150 (2011).

39. Jauregui, L. A. *et al.* Electrical control of interlayer exciton dynamics in atomically thin heterostructures. *Science*. **366**, 870–875 (2019).
40. Rhodes, D., Chae, S. H., Ribeiro-Palau, R. & Hone, J. Disorder in van der Waals heterostructures of 2D materials. *Nat. Mater.* **18**, 541–549 (2019).
41. Rezk, A. R. *et al.* Acoustically-Driven Trion and Exciton Modulation in Piezoelectric Two-Dimensional MoS₂. *Nano Lett.* **16**, 849–855 (2016).
42. Jones, A. M. *et al.* Spin-layer locking effects in optical orientation of exciton spin in bilayer WSe₂. *Nat. Phys.* **10**, 130–134 (2014).
43. Lindlau, J. *et al.* The role of momentum-dark excitons in the elementary optical response of bilayer WSe₂. *Nat. Commun.* **9**, 2586 (2018).
44. Kamban, H. C. & Pedersen, T. G. Interlayer excitons in van der Waals heterostructures: Binding energy, Stark shift, and field-induced dissociation. *Sci. Rep.* **10**, 5537 (2020).
45. Fu, W. *et al.* Phononic integrated circuitry and spin–orbit interaction of phonons. *Nat. Commun.* **10**, 2743 (2019).
46. Mayor, F. M. *et al.* Gigahertz Phononic Integrated Circuits on Thin-Film Lithium Niobate on Sapphire. *Phys. Rev. Appl.* **15**, 014039 (2021).

Data availability statement:

The data that support the findings of this study are available from the corresponding author upon reasonable request.